Joint Petrophysical and Structural Inversion of Electromagnetic and Seismic Data Based on Volume Integral Equation Method

Tian Lan, Na Liu, *Member, IEEE*, Feng Han, *Member, IEEE*, and Qing Huo Liu, *Fellow, IEEE*

***Abstract*— A joint petrophysical and structural inversion method for electromagnetic (EM) and seismic data based on the volume integral equation (VIE) is proposed in this paper. In the forward EM problem, only the contrast of conductivity is solved by the electric field integral equation method. However, in the forward seismic problem, both the contrasts of velocity and mass density are solved by the combined field VIE method. Both forward solvers are accelerated by the fast Fourier transform. In the inversion problem, by using the petrophysical equations about the porosity and saturation and applying the chain rule, we fuse the EM and seismic data and construct the joint petrophysical inversion equations, which can be solved by the variational Born iteration method. Then, in order to further enhance the reconstructed results of the joint petrophysical inversion, we enforce the structural similarity constraint between porosity and water saturation and add the cross-gradient function to the joint petrophysical inversion cost function. Two typical geophysical models based on the remote sensing measurement are used to validate the proposed methods. One is the cross-well model, and the other is the marine surface exploration model. The advantage of the joint inversion compared with the separate inversion is evaluated based on the resolution and the data misfits of the reconstructed profiles as well as the antinoise ability.**

***Index Terms*— Joint inversion, petrophysical, structural similarity, variational Born iteration method (VBIM).**

I. Introduction

ELECTROMAGNETIC (EM) and seismic full-waveform inversions play an important role in geophysical exploration and reservoir monitoring [1]–[3]. Due to their own advantages and disadvantages, these two methods are employed in different scenes. EM data are mainly used to invert for the conductivity distribution in the underground region [4], which is widely adopted in metal mine and ground water detection. However, the propagation of low-frequency EM wave in the earth is diffusive and suffers from high attenuation. The reconstructed conductivity profile has a low image resolution. On the contrary, seismic waves in the earth have little attenuation, thus seismic inversion results have much higher structural resolution than EM inversion results. Unfortunately, the seismic method lacks the ability to discern oil from water, which is an important issue in geophysical resource exploration. By contrast, due to the high contrast of the conductivity of water and oil, EM fields play an indispensable role to identify the fluid type. Conventionally, these two inversion processes are performed individually, and the inversion results are finally analyzed simultaneously to explain the underground structural and conducting information. Therefore, the joint inversion of EM and seismic data is of great concern to researchers.

The idea of the joint inversion was first proposed in [5] and acquired a great development in the following decades. There are mainly two types of joint inversion methods. One is to invert for the petrophysical parameters [6]–[8], such as porosity and fluid saturations, to link different geophysical parameters, like conductivity in EM problems and velocity and mass density in seismic problems. The links are based on petrophysical equations. For example, Archie's equation [9] and Waxman and Smits' equation [10] build the relationships between porosity, water saturation, and conductivity. Gassmann's equations [11] realize the relationship between velocity, mass density, porosity, and fluid saturations. The petrophysical relationships can be obtained by the core analysis in the exploration region. Although the petrophysical equations are empirical and problem-dependent [12], they are widely adopted in geophysical engineering due to their strong constraint and good performance. The update of the inverse parameters is simultaneous in this petrophysics-based joint inversion. The second joint inversion method is based on the assumption that there is a structural similarity between the different physical parameters [12]–[14], which is reasonable in the real world. By using the cross-gradient function to link different physical fields [13], the structures of different parameters in the same geology will be kept similar when the cross-gradient function is minimized. Different from the petrophysics-based method, the constraint by the structural similarity is weak. Because the joint structural inversion method is more general and problem-independent [15], it can be easily applied to various kinds of physical scenes [16], [17]. There are two types of updating fashions for the joint structural inversion. One is alternating [12], and the other is simultaneous [15]. On the one hand, the alternating fashion has less computation and memory storage than the

Manuscript received April 23, 2018; revised August 18, 2018; accepted September 16, 2018. Date of publication October 9, 2018; date of current version March 25, 2019. This work was supported by the National Natural Science Foundation of China under Grant 41390453, Grant 11501481, and Grant 41504120. *(Corresponding authors: Feng Han; Qing Huo Liu.)*

T. Lan, N. Liu, and F. Han are with the Department of Electronic Science, Institute of Electromagnetics and Acoustics, Xiamen University, Xiamen 361005, China (e-mail: feng.han@xmu.edu.cn).

Q. H. Liu is with the Department of Electrical and Computer Engineering, Duke University, Durham, NC 27708 USA (e-mail: qhliu@duke.edu).

Color versions of one or more of the figures in this paper are available online at http://ieeexplore.ieee.org.

Digital Object Identifier 10.1109/TGRS.2018.2871075

simultaneous fashion. On the other hand, simultaneous inversion is more robust [15]. Our previous research is based on the structural similarity [18], in which the variational Born iteration method (VBIM) is used to reconstruct the contrasts of velocity and conductivity in the 2-D layered media by the alternating fashion. However, the petrophysical parameters are not considered.

In this paper, we fuse the joint petrophysical and structural inversions by constructing a unified cost functional based on the volume integral equation (VIE) method. The direct inversion parameters are the porosity and fluid saturations. In the full-waveform inversion process, the 2-D EM forward scattering problem is formulated by electric field integral equation (EFIE) in layered media with only the contrast of conductivity taken into account [19]. But for 2-D seismic forward scattering, both the compressibility contrast and mass density contrast are included in the VIE [20]. The forward iterations for the EM and seismic scattering are achieved by the stabilized biconjugate gradient (BCGS) method and accelerated with the fast Fourier transform (FFT) [21]. However, in the inversion process, the petrophysical parameters are retrieved jointly by the VBIM. The update of the direct inversion parameters is carried out through the chain rule, which links the original VBIM equation and the variation of petrophysical equations. Then, the minimization process is carried out by conjugate gradient (CG) method. Considering the natural range of the porosity and fluid saturations, we introduce the nonlinear transform in VBIM to constrain the ranges of these two parameters during the inversion process [22]. Furthermore, we take the cross-gradient function into consideration to enforce the structure similarity between porosity and saturation and adopt the simultaneous updating fashion. The inversion results from synthetic data with two typical geophysical models are used to evaluate the performance of the separate inversion and joint inversion.

This paper is organized as follows. In Section II, we first introduce methods for forwarding EM and seismic scattering computation based on VIEs. Then, separate inversions of EM and seismic data are discussed. Joint petrophysical inversion which can be further enhanced by enforcing the structural similarity constraint between porosity and water saturation is presented in Sections II-C and II-D. In Section III, we test the performance of joint inversion methods as well as separate inversion methods with two geophysical models based on the remote sensing measurement, which are illustrated in Fig. 1. One is the cross-well model, and the other is the marine surface exploration model. Finally, conclusions and discussions are presented in Section IV.

II. Methods

A. Forward Model

In the 2-D problem, we define the computational domain Ω in the xz plane and assume all the parameters are invariant along the $\hat{y}$ direction. The electrical excitation source is along the $\hat{y}$ direction, i.e., only the $\hat{y}$ direction (TMy) wave is considered. When the transverse magnetic referring to the TMy wave propagates, the electric field exists only in $\hat{y}$ direction, while the magnetic field exists in both $\hat{x}$ and $\hat{z}$ directions.

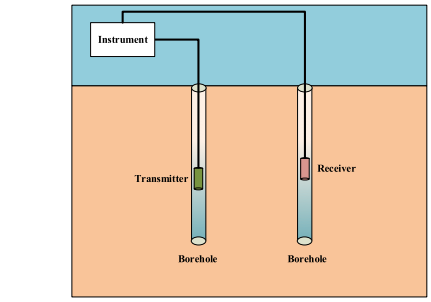

(a)

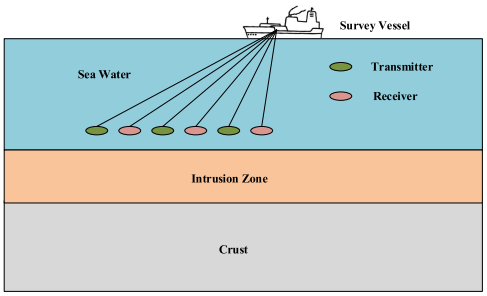

(b)

Fig. 1. Illustration of remote sensing measurements in two typical models. (a) Cross-well model, in which the transmitter and receiver are located in the two boreholes. (b) Marine surface exploration model, in which the transmitter and receiver are located near the seafloor.

For the EM problem, the scalar Helmholtz equation deduced from Maxwell's equations is

$$\left(\Delta + k_{\mathrm{EM}}^2\right) E_y = j\omega_{\mathrm{EM}}\mu_0 J_y \tag{1}$$

where ω_{EM} is the EM angular frequency, μ_0 is the permeability in free space, J_y is the EM source, and $k_{\mathrm{EM}} = \omega_{\mathrm{EM}}(\mu_0\tilde{\epsilon})^{1/2}$ represents the complex wavenumber of the EM field. We use σ expressing conductivity and ϵ expressing the real permittivity. Considering $\sigma/\omega_{\mathrm{EM}} \gg \epsilon$ in low-frequency geophysical application, the complex permittivity is

$$\tilde{\epsilon} = \epsilon + \frac{\sigma}{j\omega_{\mathrm{EM}}} \approx \frac{\sigma}{j\omega_{\mathrm{EM}}}. \tag{2}$$

For the seismic problem, the scalar acoustic approximation is used, which shows well-posedness in inverse problems [23]. Unlike our previous work [18], we no longer neglect the contrast of mass density ρ in this paper. The acoustic wave equation in frequency domain for scalar pressure p is [24]

$$\nabla \cdot \rho^{-1}\nabla p + \omega_s^2 \kappa p = -S \tag{3}$$

where ω_s is the acoustic angular frequency, κ is the compressibility, and S is the source term. The relationships of κ, ρ, velocity c, and bulk modulus K are

$$\kappa = 1/K \tag{4}$$

$$K = \rho c^2. \tag{5}$$

As we discussed in [20], the wave scattering problem in layered media can be formulated by the VIE. The total field is split into the incident and scattered field. The VIEs in general have no analytic solutions. They are first expanded

by a set of basis functions and then solved numerically. The traditional method of moments (MoM) is not always adopted to solve the discretized VIEs due to its high computation cost [25]. The computational complexity of MoM for CPU time is $O(N^3)$, and the memory requirement is $O(N^2)$, where N is the number of unknowns in the computation domain. In contrast, the iteration solver BCGS expedited by FFT only needs $O(MN \log N)$ CPU time and $O(N)$ memory [26], where M is the number of iterations.

For the reason that the mass density ρ is considered, (3) in this paper is different from (2) in [18]. Therefore, the VIE used to solve (3) in this paper is different from the EFIE used to solve (2) in [18]. In order to clarify the difference, we first give the analogy of (3) in the EM problem. When both the contrasts of permittivity and permeability in the EM scattering problem are considered, the 2-D Helmholtz equation is [27]

$$\nabla \cdot \mu^{-1} \nabla E_y + \omega^2 \epsilon E_y = j\omega J_y. \tag{6}$$

Comparing (3) with (6), we find that ρ and κ in (3) are analog of the permeability μ and the permittivity ϵ in (6), respectively. The unknown p in (3) is similar as the unknown E_y in (6). We have used the combined field VIE (CFVIE) method to solve the EM scattering problems with both the contrasts of permittivity and permeability in [20]. Therefore, all the methods in [20] can be applied to solve p in (3). The particle velocity $\mathbf{v}$ in acoustics is corresponding to $\mathbf{H}$ in 2-D EM scattering problem solved by CFVIE.

B. Separate Inversion

VBIM based on the integral equation is first proposed in [28] and employed widely in geophysical inversion [18], [29], [30]. VBIM takes the variation of the scattered field about the contrast and minimizes the cost function to update the inverse parameters [29].

For the EM model, the scattered electric field in the receivers is scalar and can be expressed as

$$E^{\text{sct}}(\mathbf{r}) = \int_{\Omega} G^{\text{EJ}}(\mathbf{r}, \mathbf{r}') \chi_{\epsilon}(\mathbf{r}') E(\mathbf{r}') d\mathbf{r}'. \tag{7}$$

Because of the approximation in (2), the contrast of permittivity in (7) can be defined as

$$\chi_{\epsilon} = \frac{\sigma - \sigma_b}{\sigma_b} \tag{8}$$

where σ is the conductivity in the computational domain, and σ_b is the conductivity of the background medium. G^{EJ} is the 2-D Green's function in homogeneous or layered media. Its derivation has been discussed in [19]. $\chi_{\epsilon}(\mathbf{r}')E(\mathbf{r}')$ is actually the equivalent electric current source in the computational domain $\mathbf{\Omega}$.

For the seismic model, the scattered pressure field in the receivers is expressed as

$$p^{\text{sct}}(\mathbf{r}) = \int_{\Omega} G^{pS_{\kappa}}(\mathbf{r}, \mathbf{r}') \chi_{\kappa}(\mathbf{r}') p(\mathbf{r}') d\mathbf{r}' - \int_{\Omega} \mathbf{G}^{pS_{\rho}}(\mathbf{r}, \mathbf{r}') \chi_{\rho}(\mathbf{r}') \mathbf{v}(\mathbf{r}') d\mathbf{r}' \tag{9}$$

where the contrast of compressibility is defined as

$$\chi_{\kappa} = \frac{\kappa - \kappa_b}{\kappa_b} \tag{10}$$

and the contrast of mass density is

$$\chi_{\rho} = \frac{\rho - \rho_b}{\rho_b}. \tag{11}$$

In (9), $G^{pS_{\kappa}}$ and $\mathbf{G}^{pS_{\rho}}$ are the 2-D Green's functions for seismic wave which are analogous to G^{EJ} and $\mathbf{G}^{\text{HM}}$ in EM problems. $G^{pS_{\kappa}}$ denotes the pressure field generated by the equivalent source $\chi_{\kappa}(\mathbf{r}')p(\mathbf{r}')$, while $\mathbf{G}^{pS_{\rho}}$ means the pressure field generated by the equivalent source $\chi_{\rho}(\mathbf{r}')\mathbf{v}(\mathbf{r}')$.

We take the variation of (7) and (9) about the contrasts and obtain

$$\delta E^{\text{sct}}(\mathbf{r}) = \int_{\Omega} G^{\text{EJ}}(\mathbf{r}, \mathbf{r}') E(\mathbf{r}') \delta\chi_{\epsilon}(\mathbf{r}') d\mathbf{r}' \tag{12}$$

$$\delta p^{\text{sct}}(\mathbf{r}) = \int_{\Omega} G^{pS_{\kappa}}(\mathbf{r}, \mathbf{r}') p(\mathbf{r}') \delta\chi_{\kappa}(\mathbf{r}') d\mathbf{r}' - \int_{\Omega} \mathbf{G}^{pS_{\rho}}(\mathbf{r}, \mathbf{r}') \mathbf{v}(\mathbf{r}') \delta\chi_{\rho}(\mathbf{r}') d\mathbf{r}' \tag{13}$$

where E, p, and $\mathbf{v}$ are the total fields in the forward computation. This is different from our previous work [18], in which the incident fields are used to approximate the total fields, i.e., the Born approximation is adopted [18], [29]. The Born approximation is only suitable for weak scattering. In this paper, we directly use the total fields in (12) and (13). Consequently, the strong scattering problems can also be computed. δE^{sct} and δp^{sct} are the misfits of the scattered fields between the measured data and the computed data similar to that in our previous work [18]. The inversion process in the VBIM is to obtain $\delta\chi_{\epsilon}$ as well as $\delta\chi_{\kappa}$ and $\delta\chi_{\rho}$ by minimizing the cost function, which is defined as

$$F_q(\delta\boldsymbol{\chi}_q) = \left\| \delta\mathbf{f}^{\text{sct}}_{q-1} - \mathbf{L}_{q-1}\delta\boldsymbol{\chi}_q \right\|^2 + \gamma^2 \frac{\left\| \delta\mathbf{f}^{\text{sct}}_{q-1} \right\|^2}{\left\| \delta\boldsymbol{\chi}_{q-1} \right\|^2} \left\| \delta\boldsymbol{\chi}_q \right\|^2 \tag{14}$$

where $\| \cdot \|$ means the L2 norm, q is the iteration index, $\mathbf{f}^{\text{sct}}$ is the scattered electric field or scattered pressure field, γ is the fixed regularization factor, and $\boldsymbol{\chi}$ is the contrast which can be $\boldsymbol{\chi}_{\epsilon}$ or the combination of $\boldsymbol{\chi}_{\kappa}$ and $\boldsymbol{\chi}_{\rho}$. In each iteration, we compute the scattered field from the newest inverted parameters. Then, we update $\delta\mathbf{f}^{\text{sct}}_{q-1}$ by subtracting the computed scattered field from the measured scattered field. $\|\delta\mathbf{f}^{\text{sct}}_{q-1}\|^2 / \|\delta\boldsymbol{\chi}_{q-1}\|^2$ is the self-adaptive regularization factor, which can decrease along with the inversion process according to the change of $\delta\mathbf{f}^{\text{sct}}$ and $\delta\boldsymbol{\chi}$ in the previous step. The least square problem of (14) is transformed into [18]

$$\left(\mathbf{L}^{\dagger}_{q-1}\mathbf{L}_{q-1} + \frac{\gamma^2 \left\| \delta\mathbf{f}^{\text{sct}}_{q-1} \right\|^2}{\left\| \delta\boldsymbol{\chi}_{q-1} \right\|^2} \mathbf{I} \right) \delta\boldsymbol{\chi}_q = \mathbf{L}^{\dagger}_{q-1}\delta\mathbf{f}^{\text{sct}}_{q-1} \tag{15}$$

where $\dagger$ means the complex conjugate and transpose operation. This equation can be solved by the CG method [31] to obtain $\delta\boldsymbol{\chi}_q$. Once $\delta\boldsymbol{\chi}_q$ is obtained, we update $\boldsymbol{\chi}$ and perform the forward computation to compute the total field E in (12), and p and $\mathbf{v}$ in (13). Then, $\mathbf{f}^{\text{sct}}_q$ and $\mathbf{L}_q$ in (15) can be updated to obtain $\delta\boldsymbol{\chi}_{q+1}$. Because the inverse parameters are

not frequency-dependent, the iteration can be easily applied for the simultaneous multifrequency inversion.

Note that there are four criteria to terminate the iteration in the inversion process by VBIM as follows.

1) Data misfit is less than the threshold.
2) Decrease of data misfit between two iterations is smaller than a threshold.
3) The data misfit in the latest iteration is bigger than the previous one.
4) The change of inversion parameters is smaller than a threshold.

To quantitatively evaluate the performance of inversion, we define the model misfit as

$$\mathrm{Err}_{\mathrm{model}} = \frac{\|\mathbf{m}_{\mathrm{inv}} - \mathbf{m}_{\mathrm{true}}\|}{\|\mathbf{m}_{\mathrm{true}}\|} \tag{16}$$

where $\mathbf{m}_{\mathrm{inv}}$ is the inverted parameter in the discretized computational domain, and $\mathbf{m}_{\mathrm{true}}$ is the true parameters distribution in that region.

We also define the data misfit as

$$\mathrm{Err}_{\mathrm{data}} = \frac{\left\|\mathbf{f}^{\mathrm{sct}}_{\mathrm{inv}} - \mathbf{f}^{\mathrm{sct}}_{\mathrm{meas}}\right\|}{\left\|\mathbf{f}^{\mathrm{sct}}_{\mathrm{meas}}\right\|} \tag{17}$$

where $\mathbf{f}^{\mathrm{sct}}_{\mathrm{inv}}$ in the receivers is the scatted field computed from the inverted parameter $\mathbf{m}_{\mathrm{inv}}$, and $\mathbf{f}^{\mathrm{sct}}_{\mathrm{meas}}$ is the scattered field from measurement.

C. Joint Petrophysical Inversion

For joint petrophysical inversion, we build relationships between geophysical parameters and petrophysical parameters based on the petrophysical equations. In the following, we will see that the petrophysical parameters can determine the geophysical parameters uniquely, while geophysical parameters can match countless compositions of the petrophysical parameters.

For the EM parameter, we adopt Archie's equation [8], [9]

$$\sigma = \frac{1}{a}\sigma_w \phi^m S_w^n \tag{18}$$

where σ_w is the conductivity of the formation saline water, a is the tortuosity factor, ϕ is the porosity, m is the exponent of porosity, S_w is the water saturation, and n is the exponent of saturation. Then, we have the variational expression about (18)

$$\delta\sigma = \frac{1}{a}\sigma_w\left(m\phi^{m-1}S_w^n\delta\phi + n\phi^m S_w^{n-1}\delta S_w\right). \tag{19}$$

For seismic parameters, we use Gassmann's equations [8], [11]. In virtue of the acoustic approximation, we only consider compressional wave (P-wave) and neglect the shear modulus in this paper. In this case, we assume an oil–water system. The gas saturation S_g is omitted. Therefore, Gassmann's equations are given as

$$K = (1-\beta)K_{\mathrm{ma}} + \beta^2 M \tag{20a}$$

$$M = \left(\frac{\beta-\phi}{K_{\mathrm{ma}}} + \frac{\phi}{K_f}\right)^{-1} \tag{20b}$$

$$K_f = \left(C_w\frac{S_w}{K_w} + C_o\frac{S_o}{K_o}\right)^{-1} \tag{20c}$$

$$\rho = (1-\phi)\rho_{\mathrm{ma}} + \phi(S_w\rho_w + S_o\rho_o) \tag{20d}$$

where $S_o = 1.0 - S_w$ is the oil saturation, K_{ma} and ρ_{ma} are the bulk modulus and the density of the matrix (solid or grain), K_w is the bulk modulus for water, and K_o is the bulk modulus for oil. C_w and C_o are correction terms for water and oil, which are usually equal to 1 [15]. The Biot coefficient β satisfies

$$\beta = \begin{cases} \phi/\phi_c, & 0 \le \phi \le \phi_c \\ 1, & \phi > \phi_c \end{cases} \tag{21}$$

where ϕ_c is the critical porosity. We also make the variation of (20) about ϕ and S_w

$$\begin{aligned}\delta K = &\left[\phi\beta^2 M^2\left(\frac{C_o}{K_o} - \frac{C_w}{K_w}\right)\right]\delta S_w \\ &+ \left(2\beta M - K_{\mathrm{ma}} - \frac{\beta^2 M^2}{K_{\mathrm{ma}}}\right)\frac{\partial\beta}{\partial\phi}\delta\phi \\ &- \beta^2 M^2\left(\frac{1}{K_f} - \frac{1}{K_{\mathrm{ma}}}\right)\delta\phi \end{aligned} \tag{22a}$$

$$\delta\rho = (S_w\rho_w + S_o\rho_o - \rho_{\mathrm{ma}})\delta\phi + \phi(\rho_w - \rho_o)\delta S_w \tag{22b}$$

where $\partial\beta/\partial\phi$ is

$$\frac{\partial\beta}{\partial\phi} = \begin{cases} 1/\phi_c, & 0 \le \phi \le \phi_c \\ 0, & \phi > \phi_c. \end{cases} \tag{23}$$

The last step is to obtain the variational expressions of (4), (8), (10), and (11)

$$\delta\kappa = -\frac{1}{K^2}\delta K \tag{24}$$

$$\delta\chi_\epsilon = \frac{1}{\sigma_b}\delta\sigma \tag{25}$$

$$\delta\chi_\kappa = \frac{1}{\kappa_b}\delta\kappa \tag{26a}$$

$$\delta\chi_\rho = \frac{1}{\rho_b}\delta\rho. \tag{26b}$$

Combining (12), (19), and (25) with the chain rule, we can obtain the variational equation of the scattered electric field about porosity and water saturation, which is expressed in the discrete form with matrix

$$\delta\mathbf{E}^{\mathrm{sct}}_{q-1} = \mathbf{L}^{\mathrm{EM}}_{q-1}\begin{bmatrix}\delta\phi \\ \delta\mathbf{S}_w\end{bmatrix}. \tag{27}$$

By following the similar procedure, we combine (13), (22), (24), and (26) and obtain the discrete form of the variational equation of the scattered pressure field about porosity and water saturation, which is expressed as

$$\delta\mathbf{p}^{\mathrm{sct}}_{q-1} = \mathbf{L}^{S}_{q-1}\begin{bmatrix}\delta\phi \\ \delta\mathbf{S}_w\end{bmatrix}. \tag{28}$$

We can assemble (27) and (28) directly, and then the joint variational equation including EM and seismic data is

$$\begin{bmatrix}\delta\mathbf{E}^{\mathrm{sct}}_{q-1} \\ \eta\delta\mathbf{p}^{\mathrm{sct}}_{q-1}\end{bmatrix} = \begin{bmatrix}\mathbf{L}^{\mathrm{EM}}_{q-1} & \eta\mathbf{L}^{S}_{q-1}\end{bmatrix}\begin{bmatrix}\delta\phi \\ \delta\mathbf{S}_w\end{bmatrix} \tag{29}$$

where the joint petrophysical factor η is defined as

$$\eta = \frac{\left\|\delta\mathbf{E}^{\mathrm{sct}}_{q-1}\right\|}{\left\|\delta\mathbf{p}^{\mathrm{sct}}_{q-1}\right\|} \tag{30}$$

to balance the contribution of different fields during the inversion process.

We express (29) compactly as

$$\delta \mathbf{f}_{q-1}^{\mathrm{sct}} = \mathbf{L}_{q-1}\delta\boldsymbol{\psi}. \tag{31}$$

Next, similar to (14), the cost function in the joint petrophysical inversion is defined as

$$F_q(\delta\boldsymbol{\psi}_q) = \left\|\delta \mathbf{f}_{q-1}^{\mathrm{sct}} - \mathbf{L}_{q-1}\delta\boldsymbol{\psi}_q\right\|^2 + \gamma^2 \frac{\left\|\delta \mathbf{f}_{q-1}^{\mathrm{sct}}\right\|^2}{\|\delta\boldsymbol{\psi}_{q-1}\|^2}\|\delta\boldsymbol{\psi}_q\|^2. \tag{32}$$

The least square problem of (32) is transformed into

$$\left(\mathbf{L}_{q-1}^{\dagger}\mathbf{L}_{q-1} + \frac{\gamma^2\left\|\delta \mathbf{f}_{q-1}^{\mathrm{sct}}\right\|^2}{\|\delta\boldsymbol{\psi}_{q-1}\|^2}\mathbf{I}\right)\delta\boldsymbol{\psi}_q = \mathbf{L}_{q-1}^{\dagger}\mathbf{f}_{q-1}^{\mathrm{sct}}. \tag{33}$$

This equation can also be solved by the CG method as (15). Because the elements in the matrix of the left side and those in the vector of right side of (33) are complex numbers, the solution space of CG is in the complex number domain. However, the porosity and water saturation are real physical variables. Therefore, we can decouple the real and imaginary parts of (33) and reassemble the equation as

$$\mathbf{A}\delta\boldsymbol{\psi}_q = \mathbf{b} \tag{34}$$

where

$$\mathbf{A} = \begin{pmatrix} \mathrm{Re}\left(\mathbf{L}_{q-1}^{\dagger}\mathbf{L}_{q-1} + \frac{\gamma^2\left\|\delta \mathbf{f}_{q-1}^{\mathrm{sct}}\right\|^2}{\|\delta\psi_{q-1}\|^2}\mathbf{I}\right) \\ \mathrm{Im}\left(\mathbf{L}_{q-1}^{\dagger}\mathbf{L}_{q-1} + \frac{\gamma^2\left\|\delta \mathbf{f}_{q-1}^{\mathrm{sct}}\right\|^2}{\|\delta\psi_{q-1}\|^2}\mathbf{I}\right) \end{pmatrix} \tag{35}$$

$$\mathbf{b} = \begin{pmatrix} \mathrm{Re}\left(\mathbf{L}_{q-1}^{\dagger}\mathbf{f}_{q-1}^{\mathrm{sct}}\right) \\ \mathrm{Im}\left(\mathbf{L}_{q-1}^{\dagger}\mathbf{f}_{q-1}^{\mathrm{sct}}\right) \end{pmatrix}. \tag{36}$$

During the inversion process, we introduce the nonlinear transform to constrain the inverse parameter within a reasonable range. For the VBIM in this paper, this nonlinear transform and the corresponding inverse transform are [22]

$$\tilde{\psi} = \frac{\psi_{\min} + \psi_{\max}\exp(\psi)}{1+\exp(\psi)} \tag{37}$$

and

$$\psi = \log(\tilde{\psi} - \psi_{\min}) - \log(\psi_{\max} - \tilde{\psi}) \tag{38}$$

respectively, where $\psi_{\min}$ is the lower limit while $\psi_{\max}$ is the upper limit. The variational equation for (37) is

$$\delta\tilde{\psi} = \frac{(\psi_{\max} - \psi_{\min})\exp(\psi)}{[1+\exp(\psi)]^2}\delta\psi. \tag{39}$$

By this transform, the inverse parameters ψ are always constrained between $\psi_{\min}$ and $\psi_{\max}$. Therefore, the unreasonable inversion results are avoided.

D. Joint Structural Inversion

In the previous work [18], we build a cross-gradient function for χ_ϵ and χ_c and use the alternative fashion in EM and seismic VBIM joint inversion iteration. By enforcing the structural similarity between different inverse parameters, the poor inverted profile of one parameter can be improved by the good resolution of the other parameter [32]. Here, we adopt the similar strategy and also build a cross-gradient function for ϕ and S_w

$$t = \nabla\phi \times \nabla S_w \tag{40}$$

where $\times$ is the outer product operation. When the cross-gradient function is minimized, the two edges in the profile of different inverse petrophysical parameters are aligned along the same orientation. Because ϕ and S_w range from 0 to 1 without units, it is unnecessary to normalize inverse parameters as in [12]–[14]. The element of the cross-gradient function can be discretized with the central difference method [18]

$$t_{i,j} = \left(\frac{\phi_{i,j+1} - \phi_{i,j-1}}{2\Delta z}\right)\left(\frac{S_{w;i+1,j} - S_{w;i-1,j}}{2\Delta x}\right) - \left(\frac{\phi_{i+1,j} - \phi_{i-1,j}}{2\Delta x}\right)\left(\frac{S_{w;i,j+1} - S_{w;i,j-1}}{2\Delta z}\right). \tag{41}$$

As in [18], we expand t with first-order Taylor series around t_{q-1} and neglect the high-order term

$$\mathbf{t}_q(\boldsymbol{\psi}_q) \cong \mathbf{t}_{q-1}(\boldsymbol{\psi}_{q-1}) + \mathbf{B}_{q-1}\delta\boldsymbol{\psi}_q. \tag{42}$$

Then, the cost function (32) is added with the cross-gradient function (42)

$$F_q(\delta\boldsymbol{\psi}_q) = \left\|\delta \mathbf{f}_{q-1}^{\mathrm{sct}} - \mathbf{L}_{q-1}\delta\boldsymbol{\psi}_q\right\|^2 + \gamma^2\frac{\left\|\delta \mathbf{f}_{q-1}^{\mathrm{sct}}\right\|^2}{\|\delta\boldsymbol{\psi}_{q-1}\|^2}\|\delta\boldsymbol{\psi}_q\|^2 + w^2\frac{\left\|\delta \mathbf{f}_{q-1}^{\mathrm{sct}}\right\|^2}{\|\mathbf{t}_{q-1}\|^2}\|\mathbf{t}_{q-1} + \mathbf{B}_{q-1}\delta\boldsymbol{\psi}_q\|^2 \tag{43}$$

where w is the joint structural factor. Finally, this joint petrophysical and structural cost function is transformed to a form

$$\left(\mathbf{L}_{q-1}^{\dagger}\mathbf{L}_{q-1} + \frac{\gamma^2\left\|\delta \mathbf{f}_{q-1}^{\mathrm{scat}}\right\|^2}{\|\delta\boldsymbol{\psi}_{q-1}\|^2}\mathbf{I} + \frac{w^2\left\|\delta \mathbf{f}_{q-1}^{\mathrm{sct}}\right\|^2}{\|\mathbf{t}_{q-1}\|^2}\mathbf{B}_{q-1}^{\dagger}\mathbf{B}_{q-1}\right)\delta\psi_q = \mathbf{L}_{q-1}^{\dagger}\delta\mathbf{f}_{q-1}^{\mathrm{sct}} - \frac{w^2\left\|\delta \mathbf{f}_{q-1}^{\mathrm{sct}}\right\|^2}{\|\mathbf{t}_{q-1}\|^2}\mathbf{B}_{q-1}^{\dagger}\mathbf{t}_{q-1} \tag{44}$$

which is also solved by the CG method. It should be noted that the simultaneous updating fashion will be used in this paper. Therefore, (43) is different from the cost function used for alternative updating fashion presented in our previous work [18].

III. Numerical Assessment

In this section, we will use two typical models to evaluate different inversion methods. Both models are common in geophysical application engineering and widely used in geophysical inversion method evaluations. One model is the cross-well measurement, in which the transmitters and receivers are located in the two wells. The other is the marine surface

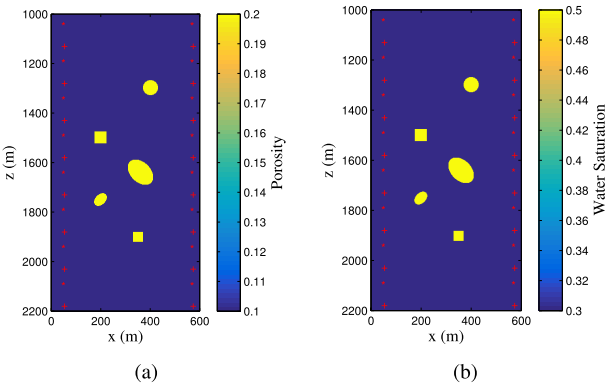

Fig. 2. Cross-well model. (a) Porosity distribution. (b) Water saturation distribution. There are 16 transmitters and 16 receivers located in the two boreholes locating at $x = 40$ m and $x = 560$ m, respectively. The transmitters distribute uniformly from $z = 1125$ m to $z = 2175$ m. The receivers distribute uniformly from $z = 1050$ m to $z = 2100$ m.

exploration model, in which the transmitters and receivers are located near the seabed. In all inversion processes mentioned below, we use the nonlinear transform (37) to constrain the inversion petrophysical parameters. For porosity, the constrained range is 0–0.35. For water saturation, the range is 0–1. The fixed regularization factor γ in (32) is chosen as 0.3. We use the initial model with the porosity and water saturation which are 0.01 larger than the background parameters.

A. Cross-Well Model

Fig. 2 shows the petrophysical distribution of a typical cross-well model. Several reservoirs with different shapes are located between two boreholes. The background of the model is homogeneous. The porosity ϕ is 0.1, and the water saturation S_w is 0.3.

We assume the petrophysical parameters of reservoirs are $\phi = 0.2$ and $S_w = 0.5$. The other petrophysical constants in the petrophysical equations (18) and (20) are mainly referred to [8]. The Archie's constants are $a = 1$, $\sigma_w = 5.5$ S/m, $m = 1.2$, and $n = 2.0$. Gassmann's constant are $\phi_c = 0.4$, $\rho_{\text{ma}} = 2560$ kg/m^3, $\rho_w = 1050$ kg/m^3, $\rho_o = 750$ kg/m^3, $K_{\text{ma}} = 32$ Gpa, $K_w = 2.81$ Gpa, and $K_o = 0.75$ Gpa. There are total 16 transmitters and 16 receivers situated in two boreholes, which are even spaced with the interval of 150 m. We use single-frequency data in this model. The EM frequency is 100 Hz, and the seismic frequency is 15 Hz. The inversion domain is 500 m $\times$ 1000 m, which is discretized with uniform square cells. The cell size is 5×5 m^2, and thus the cell number is 100×200. Unlike finite difference-based inversion methods [8], [15], we do not need the perfect matching layerlike boundary condition in VIE-based inversion method. Hence, there is no need to expand the computational domain.

First, we perform the EM-only inversion, i.e., we only apply the VBIM to (27) to reconstruct the porosity and saturation distribution in the cross-well model. After five iterations, the data misfit is 2.80% and almost keeps unchanged, so the VBIM terminates. The results are shown in Fig. 3(a) and (e). We can see the water saturation in the inversion results is closer to the true value than the porosity. This phenomenon is due to the fact that the EM data is more sensitive to the water saturation than to the porosity [8].

Similarly, we perform the inversion using only the seismic data, and the results are shown in Fig. 3(b) and (f). The inversion terminates after five iterations and the seismic data misfit is 0.67%. Compared with the results in EM-only inversion, the profile of porosity in seismic-only inversion has a much better resolution and is closer to the true model. However, the water saturation results are far away from the true values. The reason is that the seismic data is less sensitive to the water saturation compared with the porosity. Individual EM-only or seismic-only inversion cannot recover well the porosity and saturation simultaneously.

Then, we use the joint petrophysical inversion, i.e., apply the VBIM algorithm to (29), to enhance the quality of the reconstructed profiles. The results are shown in Fig. 3(c) and (g). After the VBIM inversion finishes five iterations, the data misfit for the scattered EM field is 0.75% and 0.48% for the seismic field. Compared with the results of the separate inversions shown in Fig. 3(a), (b), (e), and (f), not only the resolution of the reconstructed profiles is improved but also the values of the porosity and water saturation are closer to the true values. We quantify the model misfits of different inversion methods and list the results in Table I. The misfits of the porosity and saturation are both reduced by joint petrophysical inversion. We then further reduce the model misfits by enforcing the structural similarity constraint between porosity and water saturation in the joint inversion. The inverted profiles of joint petrophysical and structural inversion are shown in Fig. 3(d) and (h). The data misfit variations versus iteration steps for different inversion processes are shown in Fig. 5. We can see that the convergence is fast in all inversion processes.

Finally, the antinoise ability of different inversion algorithms is tested. We add Gaussian random white noises in the data of the measured scattered field. The effects of different signal-to-noise ratios (SNRs) are tested. The model misfit changes along with the different SNR values are shown in Fig. 6. We can see the model misfit increases with the decrease of SNR. We also note that the model misfits in the joint petrophysical with the structural similarity constraint are always smaller than misfits without the constraint. The model misfits for EM-only and seismic-only inversions when the noise is added are obviously larger than the misfits for joint inversions shown in Fig. 6 and thus are not displayed. The inversion results when SNR = 1 dB are shown in Fig. 4. We can see that the main reservoirs are still discernable and the small reservoirs become blur when the noise is too big. The joint petrophysical and structural inversion has the strongest antinoise ability.

B. Marine Surface Exploration Model

For the marine surface exploration model, we use the constants mainly referred to [15] in petrophysical equations (18) and (20). $a = 1$, $\sigma_w = 3.0$, $m = 0.4$, $n = 2.4$, $\phi_c = 0.4$, $\rho_{\text{ma}} = 2560$ kg/m^3, $\rho_w = 1050$ kg/m^3, $\rho_o = 750$ kg/m^3, $K_{\text{ma}} = 37$ Gpa, $K_{\text{ma}} = 2.56$ Gpa, and $K_{\text{ma}} = 0.75$ Gpa. As shown in Fig. 7, the upper layer is seawater, whose porosity

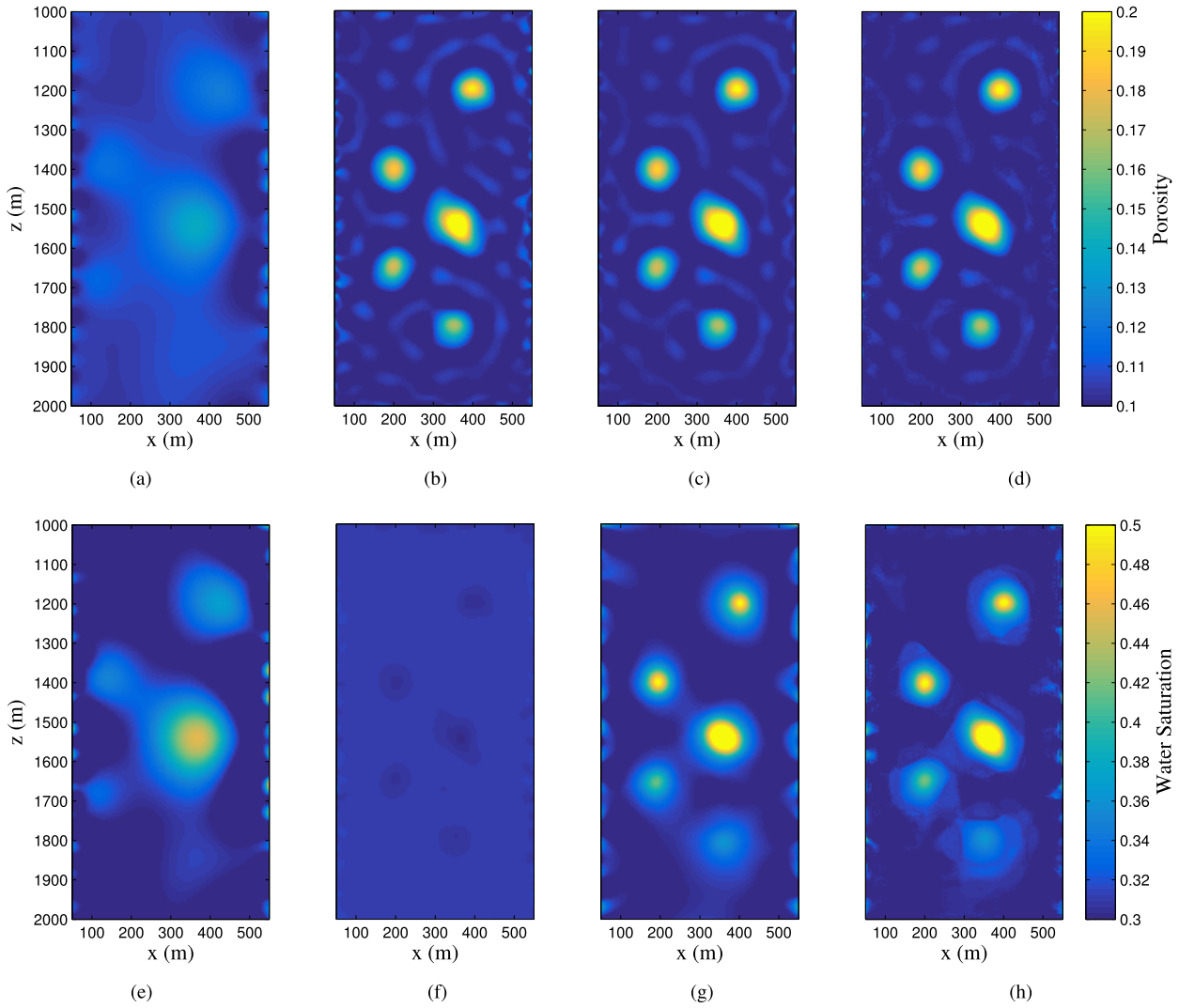

Fig. 3. Inversion results for the cross-well model when noise free. Reconstructed distributions of (a) porosity and (e) water saturation using only EM data. Reconstructed distributions of (b) porosity and (f) water saturation using only seismic data. Reconstructed distributions of (c) porosity and (g) water saturation using both EM and seismic data. Reconstructed distributions of (d) porosity and (h) water saturation using both EM and seismic data with structural constraint.

TABLE I
MODEL MISFITS FOR DIFFERENT INVERSION METHODS IN CROSS-WELL MODEL WHEN NOISE FREE

Inversion type	Model misfit(%)	
	Porosity	Water saturation
EM-only	16.319	12.174
Seismic-only	10.576	11.801
Joint petrophysical	9.975	8.257
Joint petrophysical and structural	9.626	7.657

is 1.0 and water saturation is 1.0. The middle layer is the seawater intrusion zone with the thickness of 400 m, whose porosity is 0.3 and water saturation is 1.0. The lower layer is the crust, whose porosity is 0.1 and water saturation is 0.8. Green's function in layered medium is used. There are 40 transmitters and 40 receivers located near the seabed at $z = 100$ m. The transmitters and receivers are placed alternately with the interval of 300 m. We use the multifrequency simultaneous inversion in this model. We pick EM frequency of 0.4 and 0.8 Hz, and seismic frequency of 0.4, 0.8, 1.2, and 1.6 Hz. The inversion domain in the lower layer is 10 km $\times$ 4 km, and discretized with 250 $\times$ 100 cells. The cell size is 40 $\times$ 40 m^2.

First, we invert the EM-only data for this model. After three inversion iterations, the EM data misfit is 0.97%. The results are shown in Fig. 8(a) and (b). Due to the diffusive characteristic of EM wave, the resolution is poor. Consistent with the reason that the EM data are more sensitive to the water saturation, the reconstructed profile of water saturation is better than that of porosity.

Then, we only use seismic data to obtain the petrophysical distribution and the results are shown in Fig. 8(c) and (d). In the inversion iteration, when the data misfit approaching 2.90%, it almost keeps unchanged any more. Thus, the inversion process is stopped. The inverted profile of porosity matches well with the true model. We can see that the resolution in the porosity profile is better than that in EM-only inversion, which is owing to the little attenuation of seismic wave during propagation. Nevertheless, we have a poor inversion result about the water saturation, because of the weak sensitivity of seismic data for the water saturation.

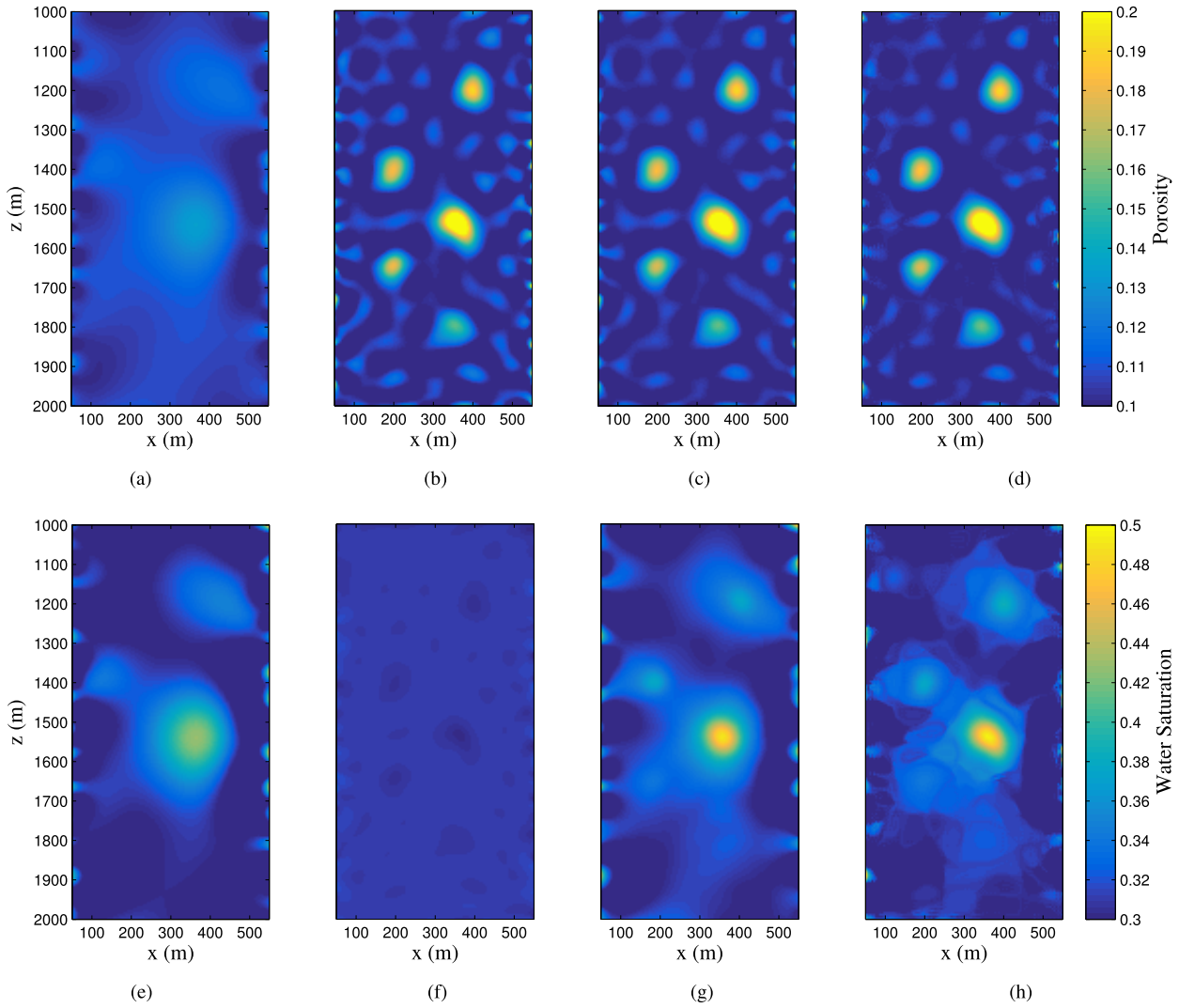

Fig. 4. Inversion results for the cross-well model when SNR = 1 dB. Reconstructed distributions of (a) porosity and (e) water saturation using only EM data. Reconstructed distributions of (b) porosity and (f) water saturation using only seismic data. Reconstructed distributions of (c) porosity and (g) water saturation using both EM and seismic data. Reconstructed distributions of (d) porosity and (h) water saturation using both EM and seismic data with structural constraint.

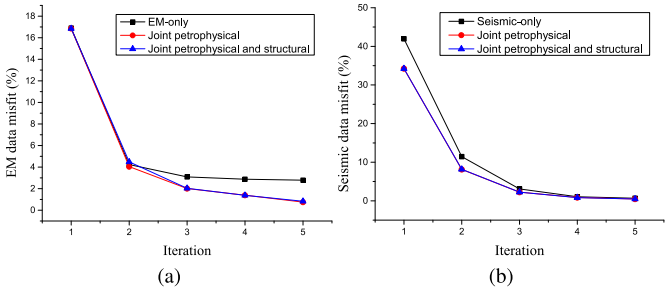

Fig. 5. Inversion convergence process in the cross-well model. (a) EM data misfits. (b) Seismic data misfits.

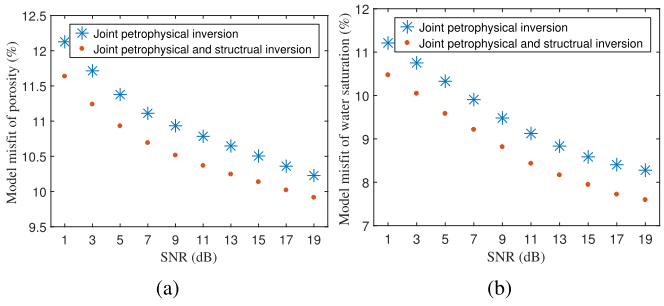

Fig. 6. Model misfits change with the SNR in the cross-well model. Model misfits of (a) porosity and (b) water saturation.

Hence, we use the joint petrophysical inversion to improve the quality of reconstructed profiles. The results are shown in Fig. 8(e) and (f). Compared with the previous inversion with single physical data, the recovered resolution and values of porosity and water saturation are improved obviously. At this time, the inversion process terminates when the EM data misfit is 0.54% and the seismic data misfit is 5.45%. In addition to the joint petrophysical method, we use structural similarity constraint to obtain better results shown in Fig. 8(g) and (h). We then compare the model misfits of these inversions and list the results in Table II. We can see that the model misfits are reduced by the joint petrophysical inversion and further decreased by introducing the structural constraint, even when the joint inversion is terminated with larger data

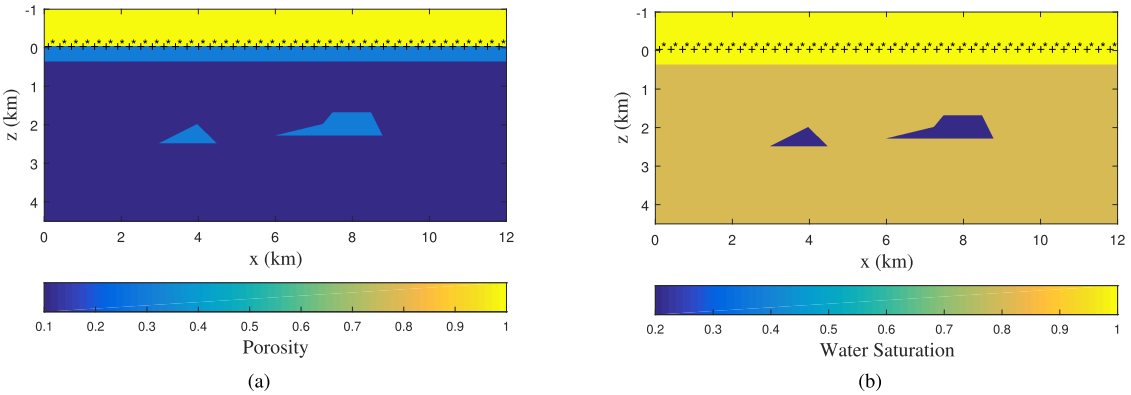

Fig. 7. Marine surface exploration model. (a) Porosity distribution. (b) Water saturation distribution. There are 40 transmitters and 40 receivers near the seabed at $z = 0.1$ km. The transmitters distribute uniformly from $x = 0$ km to $x = 11.7$ km. The receivers distribute uniformly from $x = 0.3$ km to $x = 12$ km.

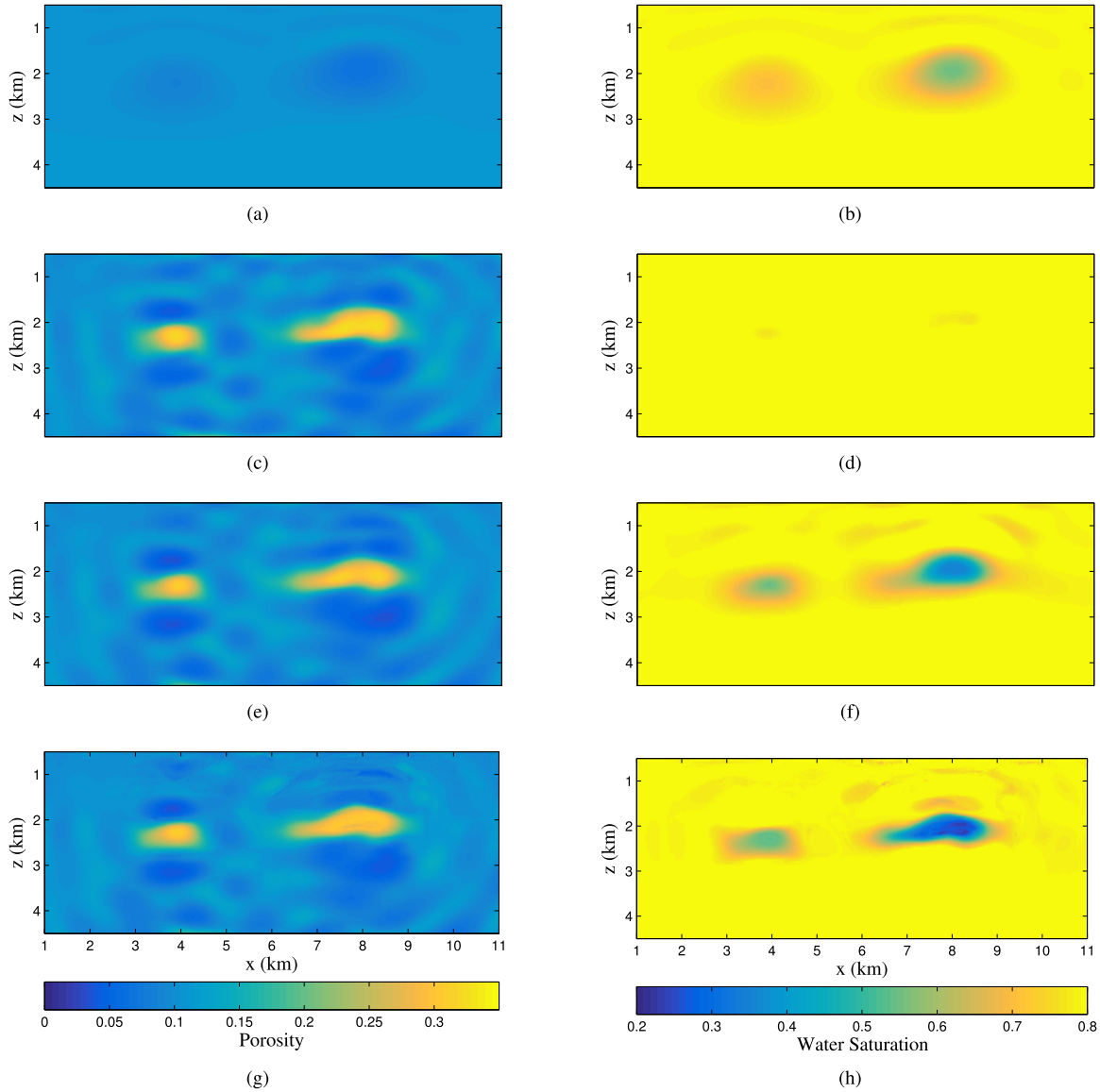

Fig. 8. Inversion results for the marine surface exploration model when noise free. Reconstructed distributions of (a) porosity and (b) water saturation using only EM data. Reconstructed distributions of (c) porosity and (d) water saturation using only seismic data. Reconstructed distributions of (e) porosity and (f) water saturation using both EM and seismic data. Reconstructed distributions of (g) porosity and (h) water saturation using both EM and seismic data with structural constraint.

misfits compared with EM-only or seismic-only inversions. The data misfit changes with iterations for different inversion processes are shown in Fig. 10. We can see that the convergence is fast in the first several steps but becomes slow when approaching the threshold. However, the convergence is stable in all inversion processes.

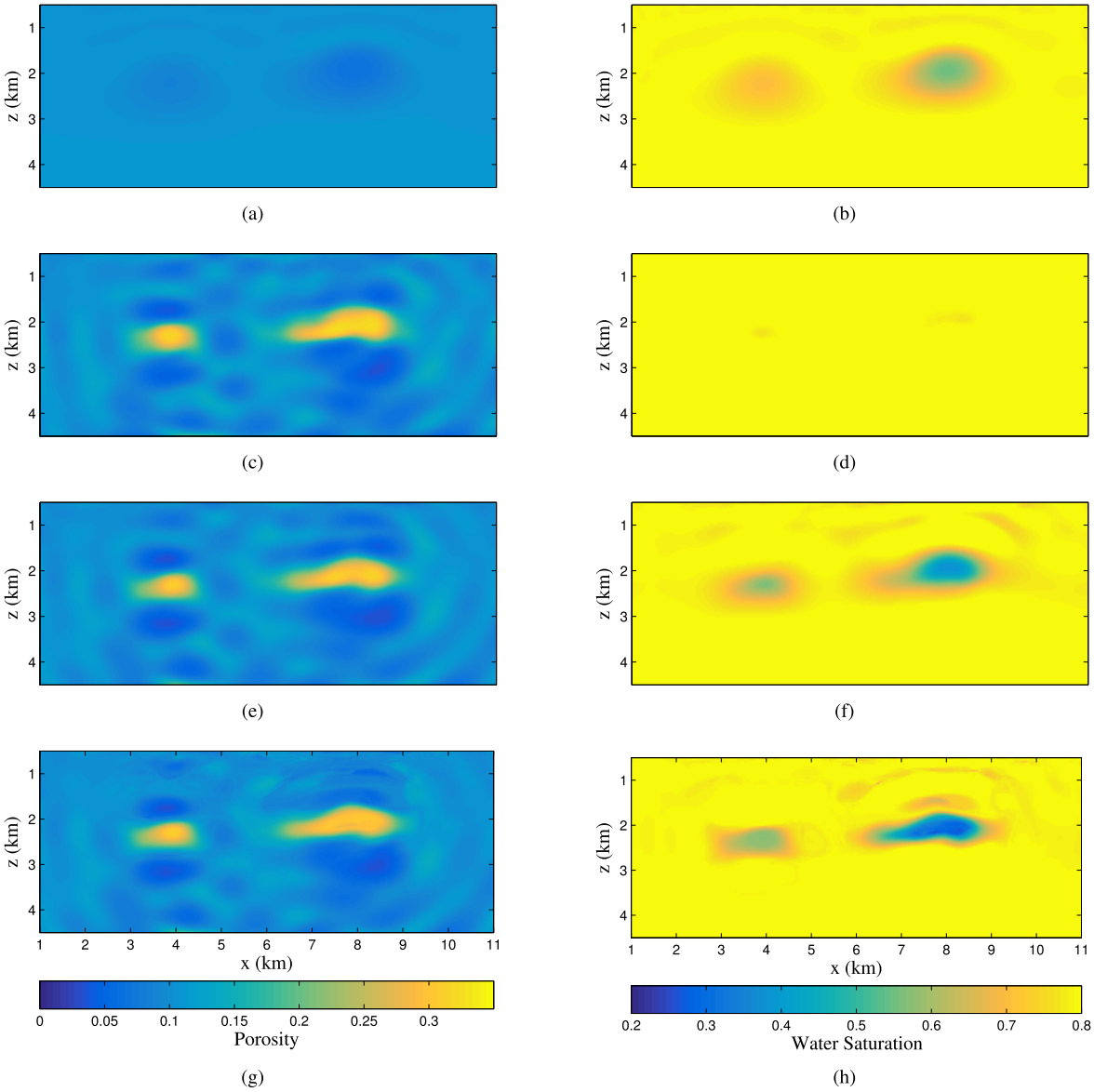

Fig. 9. Inversion results for the marine surface exploration model when SNR = 1 dB. Reconstructed distributions of (a) porosity and (b) water saturation using only EM data. Reconstructed distributions of (c) porosity and (d) water saturation using only seismic data. Reconstructed distributions of (e) porosity and (f) water saturation using both EM and seismic data. Reconstructed distributions of (g) porosity and (h) water saturation using both EM and seismic data with structural constraint.

TABLE II
MODEL MISFITS FOR DIFFERENT INVERSION METHODS IN MARINE SURFACE EXPLORATION MODEL WHEN NOISE FREE

Inversion type	Model misfit(%)	
	Porosity	Water saturation
EM-only	36.74	11.15
Seismic-only	24.49	14.19
Joint petrophysical	24.38	9.32
Joint petrophysical and structural	22.84	8.26

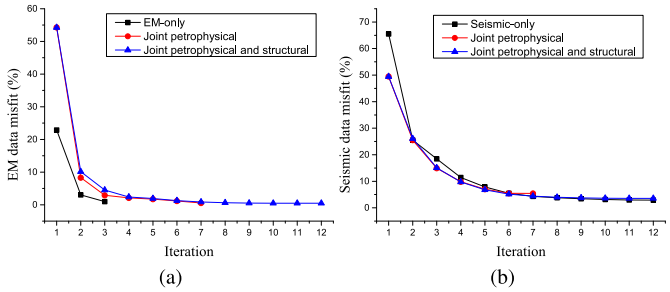

Fig. 10. Inversion convergence process in the marine surface exploration model. (a) EM data misfits. (b) Seismic data misfits.

Finally, we also test the effect of noise on the marine surface exploration model. As in the cross-well model, we use 10 different SNR values to implement four types of inversions. The model misfit versus SNR by joint inversions is shown in Fig. 11. We can see the model misfit increases as the noise increases and the performance of joint petrophysical and structural inversion is better than that without the structural constraint. Then, the inversion results when SNR = 1 dB are shown in Fig. 9. Compared with the noise-free situation in Fig. 8, the resolution becomes worse. Nevertheless, the basic information about the location of reservoir and values

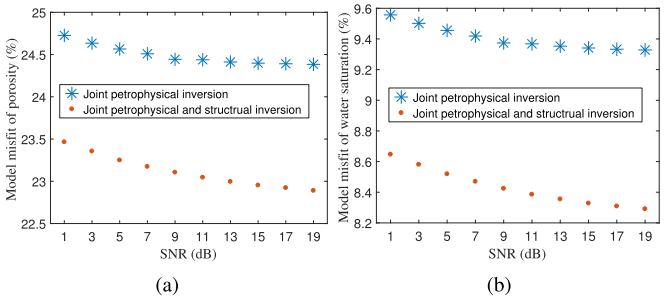

Fig. 11. Model misfits change with the SNR in the marine surface exploration model. Model misfits of (a) porosity and (b) water saturation.

of petrophysical parameters have not changed much. In the marine surface exploration model, the joint petrophysical and structural inversion have the best ability of antinoise.

IV. Conclusion

In this paper, we develop a joint petrophysical and structural inversion based on the VIE method. The key idea of this method is to take the variation of the integral equations about geophysical fields and petrophysical equations. Then, by means of the chain rule, the direct inversion parameters are changed from the geophysical parameters to petrophysical parameters. In this way, the EM and seismic data are fused to form the joint inversion cost function, which can be solved by the CG method. Considering that the porosity and water saturation have the same order of magnitudes, we can handily build the cross-gradient function without normalization to enforce the structural similarity constraint during the inversion process.

We use two typical geophysical models based on the remote sensing measurement to test our joint inversion methods. One is the cross-well model, the other is the marine surface exploration model. In both models, we first use individual physical data to perform the separate inversions. The results confirm that the EM-only inversion is more sensitive to water saturation and the seismic-only inversion has a better ability to recover porosity. Then, we use the joint petrophysical inversion method with and without the structural similarity constraint to enhance the reconstructed profiles. The results show that EM data and seismic data can compensate each others' drawbacks and enhance each others' merits. The model misfits of porosity and water saturation decrease in the joint inversion. By the introduction of structural similarity constraint, the model misfits can be further decreased. Moreover, we test the antinoise ability of the joint inversions. Even when SNR $=$ 1 dB, the locations of the reservoirs are discernable, and the values of petrophysical parameters are near the true values. This means that the proposed joint inversion methods in this paper have the strong antinoise ability and can be potentially applied in many geophysical engineering, such as petroleum explorations, reservoir characterization, and monitoring.

References

[1] S. Constable, "Ten years of marine CSEM for hydrocarbon exploration," *Geophysics*, vol. 75, no. 5, pp. A67–A81, 2010.

[2] R. G. Pratt, C. Shin, and G. J. Hick, "Gauss–Newton and full Newton methods in frequency–space seismic waveform inversion," *Geophys. J. Int.*, vol. 133, no. 2, pp. 341–362, May 1998.

[3] W. Y. Hu, A. Abubakar, and T. M. Habashy, "Simultaneous multifrequency inversion of full-waveform seismic data," *Geophysics*, vol. 74, no. 2, pp. R1–R14, 2009.

[4] S. Constable and C. S. Cox, "Marine controlled-source electromagnetic sounding: 2. The PEGASUS experiment," *J. Geophys. Res., Solid Earth*, vol. 101, no. B3, pp. 5519–5530, 1996.

[5] K. Vozoff and D. L. B. Jupp, "Joint inversion of geophysical data," *Geophys. J. Int.*, vol. 42, no. 3, pp. 977–991, 1975.

[6] G. M. Hoversten *et al.*, "Direct reservoir parameter estimation using joint inversion of marine seismic AVA and CSEM data," *Geophysics*, vol. 71, no. 3, pp. C1–C13, 2006.

[7] P. Dell'Aversana, G. Bernasconi, F. Miotti, and D. Rovetta, "Joint inversion of rock properties from sonic, resistivity and density well-log measurements," *Geophys. Prospecting*, vol. 59, no. 6, pp. 1144–1154, 2011.

[8] G. Gao, A. Abubakar, and T. M. Habashy, "Joint petrophysical inversion of electromagnetic and full-waveform seismic data," *Geophysics*, vol. 77, no. 3, pp. WA3–WA18, 2012.

[9] G. E. Archie *et al.*, "The electrical resistivity log as an aid in determining some reservoir characteristics," *Trans. AIME*, vol. 146, no. 1, pp. 54–62, 1942.

[10] M. H. Waxman *et al.*, "Electrical conductivities in oil-bearing shaly sands," *Soc. Petroleum Eng.*, vol. 8, no. 2, pp. 107–122, 1968.

[11] F. Gassmann, "Uber die elastizitat poroser medien," *Vierteljahrsschrift Naturforschenden Gesellschaft Zurich*, vol. 96, pp. 1–23, 1951.

[12] W. Hu, A. Abubakar, and T. M. Habashy, "Joint electromagnetic and seismic inversion using structural constraints," *Geophysics*, vol. 74, no. 6, pp. R99–R109, 2009.

[13] L. A. Gallardo and M. A. Meju, "Characterization of heterogeneous near-surface materials by joint 2D inversion of DC resistivity and seismic data," *Geophys. Res. Lett.*, vol. 30, no. 13, p. 1658, 2003.

[14] L. A. Gallardo and M. A. Meju, "Joint two-dimensional DC resistivity and seismic travel time inversion with cross-gradients constraints," *J. Geophys. Res., Solid Earth*, vol. 109, no. B3, p. B03311, 2004.

[15] A. Abubakar, G. Gao, T. M. Habashy, and J. Liu, "Joint inversion approaches for geophysical electromagnetic and elastic full-waveform data," *Inverse Problems*, vol. 28, no. 5, p. 55016, 2012.

[16] L. A. Gallardo, "Multiple cross-gradient joint inversion for geospectral imaging," *Geophys. Res. Lett.*, vol. 34, no. 19, pp. L19301-1–L19301-5, 2007.

[17] M. Moorkamp, B. Heincke, M. Jegen, A. W. Roberts, and R. W. Hobbs, "A framework for 3-D joint inversion of MT, gravity and seismic refraction data," *Geophys. J. Int.*, vol. 184, no. 1, pp. 477–493, 2011.

[18] T. Lan, H. Liu, N. Liu, J. Li, F. Han, and Q. H. Liu, "Joint inversion of electromagnetic and seismic data based on structural constraints using variational Born iteration method," *IEEE Trans. Geosci. Remote Sens.*, vol. 56, no. 1, pp. 436–445, Jan. 2018.

[19] L.-P. Song, E. Simsek, and Q. H. Liu, "A fast 2D volume integral-equation solver for scattering from inhomogeneous objects in layered media," *Microw. Opt. Technol. Lett.*, vol. 47, no. 2, pp. 128–134, 2005.

[20] T. Lan, N. Liu, J. Li, F. Han, and Q. H. Liu, "Two-dimensional electromagnetic scattering and inverse scattering from magneto-dielectric objects based on integral equation method," *IEEE Trans. Antennas Propag.*, to be published.

[21] X. M. Xu and Q. H. Liu, "The BCGS-FFT method for electromagnetic scattering from inhomogeneous objects in a planarly layered medium," *IEEE Antennas Wireless Propag. Lett.*, vol. 1, no. 1, pp. 77–80, 2002.

[22] M. Commer and G. A. Newman, "New advances in three-dimensional controlled-source electromagnetic inversion," *Geophys. J. Int.*, vol. 172, no. 2, pp. 513–535, Feb. 2008.

[23] J. Virieux and S. Operto, "An overview of full-waveform inversion in exploration geophysics," *Geophysics*, vol. 74, no. 6, pp. WCC1–WCC26, 2009.

[24] J. T. Fokkema and P. M. van den Berg, *Seismic Applications of Acoustic Reciprocity*. Amsterdam, The Netherlands: Elsevier, 1993.

[25] W. C. Gibson, *The Method of Moments in Electromagnetics*. Boca Raton, FL, USA: CRC Press, 2014.

[26] L. Zhang, S. He, X. Ye, W. Hu, W. Yu, and G. Zhu, "The BCGS-FFT method combined with an improved discrete complex image method for EM scattering from electrically large objects in multilayered media," *IEEE Trans. Geosci. Remote Sens.*, vol. 48, no. 3, pp. 1180–1185, Mar. 2010.

[27] A. F. Peterson, S. L. Ray, and R. Mittra, *Computational Methods for Electromagnetics*. Piscataway, NJ, USA: IEEE Press, 1998.

[28] N. Zaiping, Y. Feng, Z. Yanwen, and Z. Yerong, "Variational Born iteration method and its applications to hybrid inversion," *IEEE Trans. Geosci. Remote Sens.*, vol. 38, no. 4, pp. 1709–1715, Jul. 2000.

[29] W. Zhang and Q. H. Liu, "Three-dimensional scattering and inverse scattering from objects with simultaneous permittivity and permeability contrasts," *IEEE Trans. Geosci. Remote Sens.*, vol. 53, no. 1, pp. 429–439, Jan. 2015.

[30] Z. Yu, J. Zhou, Y. Fang, Y. Hu, and Q. H. Liu, "Through-casing hydraulic fracture evaluation by induction logging II: The inversion algorithm and experimental validations," *IEEE Trans. Geosci. Remote Sens.*, vol. 55, no. 2, pp. 1189–1198, Feb. 2017.

[31] J. R. Shewchuk *et al.*, "An introduction to the conjugate gradient method without the agonizing pain," Carnegie Mellon Univ., Pittsburgh, PA, USA, Tech. Rep. CMU-CS-94-125, Aug. 1994.

[32] M. Li, L. Liang, A. Abubakar, and P. M. Van Den Berg, "Structural similarity regularization scheme for multiparameter seismic full waveform inversion," in *Proc. SEG Tech. Program Expanded Abstracts*, 2013, pp. 1089–1094.

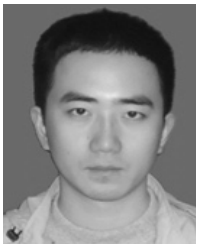

Tian Lan received the B.S. degree in electromagnetic fields and wireless technology and the M.S. degree in electromagnetic fields and microwave technology from the University of Electronic Science and Technology of China, Chengdu, China, in 2011 and 2014, respectively. He is currently pursuing the Ph.D. degree with Xiamen University, Xiamen, China.

His research interests include fast-forward solvers in electromagnetics and acoustics and joint inversion methods in multiphysical fields.

Na Liu (M'18) received the Ph.D. degree in computational mathematics from the University of Chinese Academy of Sciences, Beijing, China, in 2013.

From 2012 to 2013, she was a Visiting Student with the Department of Electrical and Computer Engineering, Duke University, Durham, NC, USA. From 2013 to 2017, she held a postdoctoral position with Xiamen University, Xiamen, China, where she is currently an Associate Professor with the Institute of Electromagnetics and Acoustics. Her research interests include computational electromagnetics, especially the fast and efficient methods for complex media and their applications in cavities and optical waveguide problems.

Feng Han (M'17) received the B.S. degree in electronic science from Beijing Normal University, Beijing, China, in 2003, the M.S. degree in geophysics from Peking University, Beijing, in 2006, and the Ph.D. degree in electrical engineering from Duke University, Durham, NC, USA, in 2011.

He is currently an Assistant Professor with the Institute of Electromagnetics and Acoustics, Xiamen University, Xiamen, China. His research interests include ionosphere remote sensing by radio atmospherics, electromagnetic full-wave inversion by integral equations, reverse time migration image, and the design of an electromagnetic detection system.

Qing Huo Liu (S'88–M'89–SM'94–F'05) received the B.S. and M.S. degrees in physics from Xiamen University, Xiamen, China, in 1983 and 1986, respectively, and the Ph.D. degree in electrical engineering from the University of Illinois at Urbana–Champaign, Champaign, IL, USA, in 1989.

From 1986 to 1988, he was a Research Assistant with the Electromagnetics Laboratory, University of Illinois at Urbana–Champaign, where he was a Post-Doctoral Research Associate from 1989 to 1990. From 1990 to 1995, he was a Research Scientist and the Program Leader with Schlumberger-Doll Research, Ridgefield, CT, USA. From 1996 to 1999, he was an Associate Professor with New Mexico State University, Las Cruces, NM, USA. Since 1999, he has been with Duke University, Durham, NC, USA, where he is currently a Professor of electrical and computer engineering. He has authored over 400 papers in refereed journals and 500 papers in conference proceedings. His research interests include computational electromagnetics and acoustics, inverse problems, and their applications in nanophotonics, geophysics, biomedical imaging, and electronic packaging.

Dr. Liu is a Fellow of the Acoustical Society of America, Electromagnetics Academy, and the Optical Society of America. He was a recipient of the 1996 Presidential Early Career Award for Scientists and Engineers from the White House, the 1996 Early Career Research Award from the Environmental Protection Agency, the 1997 CAREER Award from the National Science Foundation, and the 2017 ACES Technical Achievement Award. He served as a Guest Editor for the PROCEEDINGS of the IEEE. Since 2015, he has been the Founding Editor-in-Chief of the new IEEE JOURNAL ON MULTISCALE AND MULTIPHYSICS COMPUTATIONAL TECHNIQUES. From 2014 to 2016, he served as an IEEE Antennas and Propagation Society Distinguished Lecturer. He serves as the Deputy Editor-in-Chief for the *Progress in Electromagnetics Research*, an Associate Editor of the IEEE TRANSACTIONS ON GEOSCIENCE AND REMOTE SENSING, and an Editor of the *Journal of Computational Acoustics*.